Available online at www.sciencedirect.com
ScienceDirect
International Journal of Heat and Fluid Flow 29 (2008) 18–34
International Journal of HEAT AND FLUID FLOW
www.elsevier.com/locate/ijhff

Large-eddy simulation of film cooling flows at density gradients

P. Renze *, W. Schröder, M. Meinke

Aerodynamisches Institut, RWTH Aachen, Wüllnerstr. zw. 5 u. 7, 52062 Aachen, Germany

Received 23 December 2006; received in revised form 18 June 2007; accepted 12 July 2007
Available online 1 November 2007

Abstract

The present paper investigates the impact of the velocity and density ratio on the turbulent mixing process in gas turbine blade film cooling. A cooling fluid is injected through an inclined pipe at $\alpha = 30°$ into a turbulent boundary layer at a freestream Reynolds number of $Re_\infty = 400{,}000$. This jet-in-a-crossflow (JICF) problem is investigated using large-eddy simulations (LES). The governing equations comprise the Navier–Stokes equations plus additional transport equations for several species to simulate a non-reacting gas mixture. That is, gases of different density are effused into an air crossflow at a constant temperature. An efficient large-eddy simulation method for low subsonic flows based on an implicit dual time-stepping scheme combined with low Mach number preconditioning is applied. The comparison of the numerical findings with experimental velocity data from two-component particle-image velocimetry (PIV) measurements shows an excellent agreement. The results evidence the dynamics of the flow field in the vicinity of the jet hole, i.e., the recirculation region and the inclination of the shear layers, to be mainly determined by the velocity ratio. However, evaluating the cooling efficiency downstream of the jet hole the mass flux ratio proves to be the dominant similarity parameter, i.e., the density ratio of the jet and crossflow fluid has to be considered.

Keywords: LES; Jet-in-a-crossflow; Film cooling; Density ratio; Velocity ratio; Cooling efficiency

1. Introduction

In modern gas turbines film cooling mechanisms protect the turbine components from the thermal stresses resulting from the exposure to the hot gas stream. Since the technical design process of film cooling systems depends on the exact knowledge of the generated flow field, a detailed understanding of the flow physics is a must to improve existing cooling techniques.

In the present case, the cooling film is generated by an injection of a cooling fluid through a row of staggered holes. The flow field resulting from the interaction of the inclined cooling jet and the turbulent boundary layer is governed by complex vortex dynamics. The outer field is dominated by a counter-rotating vortex pair (CVP), which is the leading mechanism in the mixing process between the hot gas and the coolant.

Due to the high impact of film cooling on the thermal efficiency of turbines a wide range of experimental investigations on this matter can be found in the literature. Andreopoulus and Rodi (1984) measured the flow field at different velocity ratios using hot-wire probes. In a recent study Plesniak and Cusano (2005) provided a detailed analysis of the evolution of the large-scale vertical structures that dominate the jet-crossflow interaction using Laser-Doppler velocimetry (LDV). An extensive study of the effect of the density ratio has been presented by Goldstein et al. (1974). In a following investigation (Pedersen et al., 1977) studied the impact of this parameter applying the heat-mass transfer analogy. They reported a strong influence of the density ratio on the local film cooling effectiveness by measuring the concentration of a high density cooling gas along a plate. Measurements of cryogenically cooled jets with thermocouple arrangements have been performed by Pietrzyk et al. (1990) and Sinha et al. (1991). Pietrzyk et al. (1990) measured the turbulent intensities at different density ratios and in the latter article the cooling

* Corresponding author. Tel.: +49 241 8095410; fax: +49 241 8092257.
E-mail address: p.renze@aia.rwth-aachen.de (P. Renze).

0142-727X/$ - see front matter © 2007 Elsevier Inc. All rights reserved.
doi:10.1016/j.ijheatfluidflow.2007.07.010

effectiveness was found to be improved with increasing density ratio.

Most numerical investigations of the JICF problem are based on Reynolds-averaged Navier–Stokes equations (e.g., Hoda and Acharya, 2000) or the systematic study of film cooling physics by Walters and Leylek (2000). However, since the JICF problem is influenced by the interaction of wall-bounded and free turbulence and the resulting flow field possesses strongly curved streamlines, most standard turbulence models like zero-, one-, or two-equation models fail to correctly predict the resulting flow field. Gustafsson and Johansson (2006) discussed numerical simulations of effusion cooling using Reynolds Stress Models (RSM) and found them to be superior to a k-ε or the SST-k-ω model. In a recent study (Muldoon and Acharya, 2006) compared the performance of a standard k-ε model in film cooling with Direct Numerical Simulation (DNS) results. In this thorough study modifications are presented to reduce the errors in the eddy viscosity of the k-ε model. In a series of papers (Bernsdorf et al., 2006 and Burdet et al., 2005) reported on the development of a film cooling model for RANS especially adjusted to the JICF problem. The data for adapting the model is based on particle-image velocimetry (PIV) measurements.

A more general approach to investigate JICF problems is the large-eddy simulation (LES) technique. Such an analysis was performed, for instance, by Tyagi and Acharya (2003). In this work an inclined jet is injected into a turbulent boundary layer. An LES study that includes an accurate treatment of the incoming turbulent boundary layer and a plenum area was performed by Guo et al. (2006), who investigated among other issues the effects of the inclination angle and blowing ratio on the flow field. In Iourokina and Lele (2006) a similar study has been reported based on likewise ideas concerning the geometry and the numerical set-up as in the analysis discussed in the prior publications by Guo et al. (2003a, 2004, 2003b, 2006).

The impact of the jet hole shape on the cooling efficiency of film cooling flows has been investigated using LES by Renze et al. (2007).

In the present paper the impact of the density ratio between coolant and crossflow is analyzed by LES and compared with experimental data. Preliminary work on this subject has been reported by Renze et al. (2006). According to Pietrzyk et al. (1990) there are three different ways to vary the density ratio parameter: a heated free-stream flow, cryogenically cooled injectant flow, and foreign gas injection. The first two options require very complex and expensive wind tunnel measurements that are, however, desirable to validate to a certain extent the numerical findings. Since those experimental data are not available, whereas measurements at a higher density coolant were performed in Jessen et al. (in press), the density ratio parameter is studied in this investigation by the heat-mass transfer analogy, i.e., a foreign gas (CO_2) jet is injected into an air crossflow. To be more precise, to analyze the impact of the density ratio two cooling fluids are considered, air and CO_2, both of which interact with an air crossflow.

The paper is organized as follows. After a succinct description of the governing equations and the numerical method the multi-species mixing is validated by simulating a propane (C_3H_8) jet in coflowing air. Subsequently, the film cooling flow configuration and the boundary conditions are presented. In Section 8 the flow structures of a round jet-in a crossflow are analyzed and the impact of the velocity ratio and the density ratio will be studied in detail. The findings of the numerical simulations will be compared with two-component particle-image velocimetry (PIV) measurements of Jessen et al. (in press). Finally, the cooling efficiency will be evaluated.

2. Governing equations

The simulation of a turbulent and non-reacting multi-component flow is considered. The governing equations are the Navier–Stokes equations including the conservation equations for the partial densities ϱ_n of $N-1$ species, where N is the total number of different species. In tensor notation and in terms of dimensionless conservative variables the equations read

$$\frac{\partial \boldsymbol{Q}}{\partial t} + (\boldsymbol{F}^{\mathrm{C}}_{\beta} - \boldsymbol{F}^{\mathrm{D}}_{\beta})_{,\beta} = 0, \quad \boldsymbol{Q} = [\varrho_n, \varrho, \varrho u_\alpha, \varrho E]^{\mathrm{T}}, \tag{1}$$

where $\boldsymbol{Q}$ is the vector of the conservative variables and $\boldsymbol{F}^{\mathrm{C}}_{\beta}$ denotes the vector of the convective and $\boldsymbol{F}^{\mathrm{D}}_{\beta}$ that of the diffusive fluxes

$$\boldsymbol{F}^{\mathrm{K}}_{\beta} - \boldsymbol{F}^{\mathrm{D}}_{\beta} = \begin{pmatrix} \varrho_n u_\beta \\ \varrho u_\beta \\ \varrho u_\alpha u_\beta + p\delta_{\alpha\beta} \\ u_\beta(\varrho E + p) \end{pmatrix} + \frac{1}{Re} \begin{pmatrix} j_{n\beta} \\ 0 \\ \sigma_{\alpha\beta} \\ u_\alpha \sigma_{\alpha\beta} + q_\beta \end{pmatrix}. \tag{2}$$

The stress tensor $\sigma_{\alpha\beta}$ is written as a function of the strain rate tensor $S_{\alpha\beta}$

$$\sigma_{\alpha\beta} = -\nu 2\left(S_{\alpha\beta} - \frac{1}{3} S_{\gamma\gamma}\delta_{\alpha\beta}\right) \quad \text{with} \quad S_{\alpha\beta} = \frac{1}{2}(u_{\alpha,\beta} + u_{\beta,\alpha}). \tag{3}$$

The mass diffusion $j_{n\beta}$ is described by Fick's law

$$j_{n\beta} = -\frac{\varrho \mathscr{D}_n}{Sc_0} Y_{n,\beta}, \tag{4}$$

where Y_n is the mass fraction of the species n, $\mathscr{D}_n$ is the diffusion coefficient computed via mixing rules from the binary diffusion coefficients, $Sc_0 = \nu_0/\mathscr{D}_0$ is the Schmidt number, and the subscript 0 indicates the reference state of the mixture. Fourier's law of heat conduction is used to compute the heat flux q_β

$$q_\beta = -\frac{k}{Pr_0(\gamma_0 - 1)} T_{,\beta}, \tag{5}$$

where Pr is the Prandtl number. The system is closed using the equation of state for a mixture of ideal gases

$$p = \sum_n p_n \quad \text{with} \quad p_n = \frac{T}{\gamma_0}\varrho_n R_n, \tag{6}$$

where γ is the ratio of specific heats, T the temperature, p the pressure, and R the gas constant.

All transport coefficients are assumed to be a function of the temperature, e.g., the coefficient of heat conductivity k reads

$$\ln k_n^* = \sum_{i=1}^{5} a_{i\,n}^* (\ln T^*)^{i-1}. \tag{7}$$

The superscript * denotes dimensional values. The values of the transport coefficients for the mixture of the species are determined according to the mixing rules of Wilke (1950) and Bird et al. (1960), likewise for the diffusion coefficient and the viscosity and according to Mathur et al. (1967) for the heat conductivity. In the mixing rule for the diffusion coefficient $\mathscr{D}_n$, the pressure dependence is taken into account.

3. Numerical method

The discretization of the governing equations is based on a mixed central-upwind AUSM (advective upstream splitting method) scheme. That is, the inertia terms are approximated by an upwind-based scheme and the pressure terms are discretized using a centered 5-point low dissipation stencil. The large-eddy simulations are carried out using the MILES technique as reported by Fureby and Grinstein (1999, 2002) to represent the effect of the non-resolved subgrid-scales. As a consequence, the intrinsic dissipation of the numerical scheme is assumed to transfer energy from the large to the small scales. Thus, it serves as a minimum implicit SGS model. An extensive study of the AUSM algorithm with different SGS models and its dependence on the grid solution has been reported by Meinke et al. (2002). A more detailed discussion of the application of the MILES technique is given in Rütten et al. (2005).

The successful use of ILES in the numerical simulation of jet flows has been recently shown by Shur et al. (2003). Here, simulations leaving out the subgrid-scale model and using upwind-based high-order differencing are carried out to predict engine jet noise. In another paper (Tucker, 2004) shows the successful use of a high-order MILES method in conjunction with RANS in near wall regions to calculate jet flows.

The temporal approximation is based on an implicit dual time-stepping scheme. A convergence acceleration of the low Mach number problem is achieved using multigrid methods and preconditioning. This dual time-stepping algorithm is described in Alkishriwi et al. (2006). A derivative with respect to the pseudo-time τ is introduced in Eq. (1)

$$\boldsymbol{\Gamma}^{-1}\frac{\partial \boldsymbol{Q}}{\partial \tau} + \frac{\partial \boldsymbol{Q}}{\partial t} + \boldsymbol{R} = 0. \tag{8}$$

The matrix of the preconditioned scheme $\boldsymbol{\Gamma}$ has been introduced by Turkel (1999) and is modified to account for the additional mass fraction equations. The quantity $\boldsymbol{R}$ represents the convective and viscous fluxes.

A 5-stage Runge–Kutta method is applied to propagate the vector of solution $\boldsymbol{Q}$ in Eq. (1) from pseudo-time level n to $n+1$

$$\boldsymbol{Q}^{(i)} = \boldsymbol{Q}^{(n)} + \alpha_i \Delta t \boldsymbol{R}^*(\boldsymbol{Q}^{(i-1)}). \tag{9}$$

For the solution at the time level t^{n+1} follows

$$\boldsymbol{Q}^{(n+1)} = \boldsymbol{Q}^{(5)}. \tag{10}$$

The superscripts i,n denote, respectively, the step index $i = 0, \ldots, 5$ and the time level, $\Delta t = t^{n+1} - t^n$ is the time step, and $\boldsymbol{R}^* = \boldsymbol{\Gamma}\boldsymbol{R}$ represents the preconditioned inviscid and viscous residual. The Runge–Kutta coefficients are $\alpha_i = (\frac{6}{24}, \frac{4}{24}, \frac{9}{24}, \frac{12}{24}, \frac{24}{24})$. They are optimized for maximum stability of a centrally discretized scheme.

4. Validation of turbulent multi-species mixing

To show the correct prediction of the turbulent mixing of two non-reacting gas species using the aforementioned numerical method a C_3H_8 jet-in coflowing air is simulated. The flow configuration matches the experiments of Schefer and Dibble (2001). In their investigation laser Rayleigh scattering is used to obtain time- and space-resolved measurements of the mixture fraction field. The velocity measurements were previously reported by Dibble et al. (1987). The measurements deliver an excellent validation data set that is available online in the experimental data archives (Barlow, 1998).

The flow configuration is sketched in Fig. 1. A propane jet at a Reynolds number based on the jet exit diameter $Re_j = 68{,}000$ is injected into coflowing air at a jet bulk velocity $u_j = 53$ m/s and a ratio of jet to air velocity of $u_{\text{jet}}/u_{\text{air}} = 5.75$.

As indicated in Fig. 1 boundary conditions based on the characteristics of the conservation equations of an inviscid fluid are applied on the lateral sides and the outlet of the computational domain. The inflow velocity of the jet is determined by the following hyperbolic-tangent profile

$$u(r) = \frac{(u_{\text{jet}} + u_{\text{air}})}{2} + \frac{(u_{\text{jet}} - u_{\text{air}})}{2}\tanh\left(\frac{R-r}{2\delta_\theta}\right), \tag{11}$$

where $\delta_\theta/R = 0.03$ is the momentum thickness scaled by the jet radius R. The propane mixture fraction distribution f in the inflow plane is determined by a likewise distribution function. To trigger the evolution of instabilities inside the shear layers, fluctuations in the form of randomly updated vortical rings are seeded into the flow via source terms as suggested by Bogey et al. (2002). Note, the initial flow region of the jet depends on the structure and strength of the inflow forcing. Especially the virtual origin and the

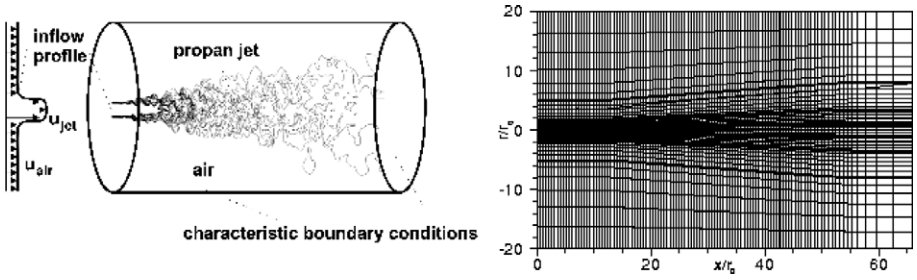

Fig. 1. Left: schematic of the computational domain and the boundary conditions for the turbulent non-reacting C_3H_8 jet, right: plan view of the computational grid in the symmetry plane; every fourth node shown.

break-up mechanism of the laminar core are susceptible to the inflow distribution. A thorough discussion of this issue is beyond the scope of this paper. However, more detailed information can be found in Bogey and Bailly (2003).

The computational grid is shown in Fig. 1 (right). To avoid the centerline singularity a cylindrical grid is constructed around a Cartesian center block. The total mesh consists of 13 blocks with $25 \times 25 \times 433$ points each yielding approximately 3.5 million grid points. The smallest grid spacing in the radial direction is located in the shear layer at $r = R$ with $\Delta r_{\min} = 0.042R$. The smallest mesh spacing in the streamwise direction is $\Delta x_{\min} = 0.13R$.

Contours of the time-averaged mixture fraction f are shown in Fig. 2. Inside the laminar potential core the propane mixture fraction f is unity. On the centerline the maximum value is preserved up to $x/R = 12$, which marks the end of the laminar core. Contours of the instantaneous mixture fraction f with mapped-on velocity contours are depicted in Fig. 3. Shortly downstream of the inlet, instabilities start to develop in the shear layers triggered by the inflow forcing. Downstream of $x/R = 12$, the shear layers roll-up and the transition to a fully turbulent state is visible.

The experimental data provided by Schefer and Dibble (2001) allows a detailed comparison with the prediction of the turbulent mixing by the jet simulation. The centerline mixture fraction decay for non-reacting turbulent jets can be correlated with the distance from the virtual origin $x_{0,1}$ using a linear function

$$1/f_{\mathrm{cl}} = C_1[(x - x_{0,1})/R], \tag{12}$$

where C_1 is the centerline decay constant and $x_{0,1}$ is a virtual origin, which is defined by the location of the onset of an approximately constant slope. The reciprocal mean mixture fraction f along the centerline is plotted in Fig. 4. It is evident that the centerline mixture fraction asymptotically approaches the similarity solution (Eq. 12). The constant C_1 is determined as 0.09. This value agrees well with the experimental results given in Table 1.

The spreading rate of the propane jet is characterized by the mixture fraction half-radius R_{fh}, which is defined as the radial location, where the mixture fraction scalar f is half of the value on the centerline. The definition reads

$$R_{\mathrm{fh}}/R = C_2[(x - x_{0,2})/R], \tag{13}$$

where C_2 is the centerline decay constant and $x_{0,2}$ is a virtual origin. The present LES predicts the spreading as $C_2 = 0.06$ (Fig. 4). The spreading rate is compared with the experimental findings in Table 1 and again, the agreement is excellent.

In Fig. 5 normalized profiles of the mean mixture fraction f and the fluctuation of the mixture fraction f' in the radial direction are shown at different axial locations $x/R = 30$ and $x/R = 60$. The data has been averaged in the circumferential direction. The radial coordinate r is scaled by the half-width radius R_{fh} for similarity reasons. The comparison of the first-order moments between the LES and the experiments is excellent. The peak fluctuations of

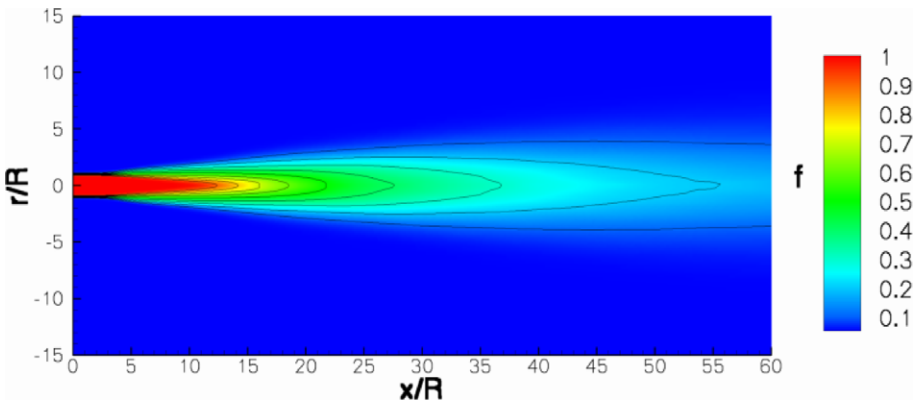

Fig. 2. Contours of the mean mixture fraction f in the jet symmetry plane.

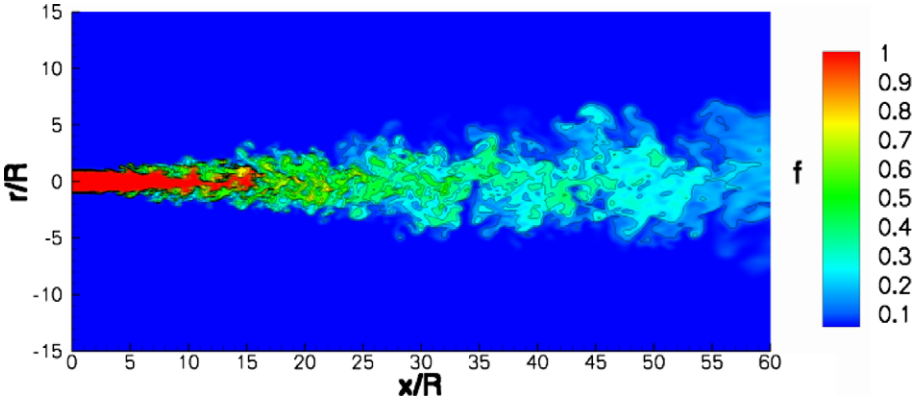

Fig. 3. Contours of the mixture fraction f at an instantaneous time level.

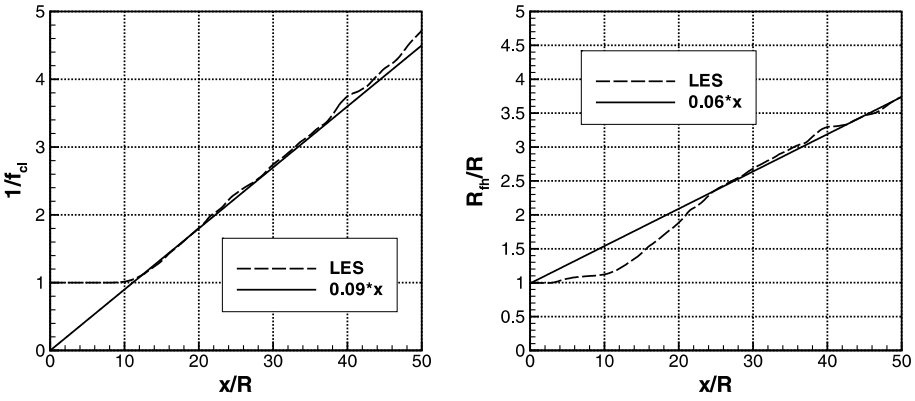

Fig. 4. Left: reciprocal mean mixture fraction f along the centerline, right: mixture fraction half-radius R_{fh} of a turbulent non-reacting C_3H_8 jet.

Table 1
Numerically and experimentally determined constants of the mean flow field

	C_1	C_2
LES	0.09	0.06
Schefer and Dibble (2001)	0.08	0.06

the mixture fraction f' are strongest at $x/R = 30$ and the LES findings do match the experiments. At $x/R = 60$ the LES curve deviates somewhat from the measurements due to the poor grid resolution in this area. However, the grid stretching near the outflow boundary is necessary. The pressure fluctuations inherent to the turbulent jet

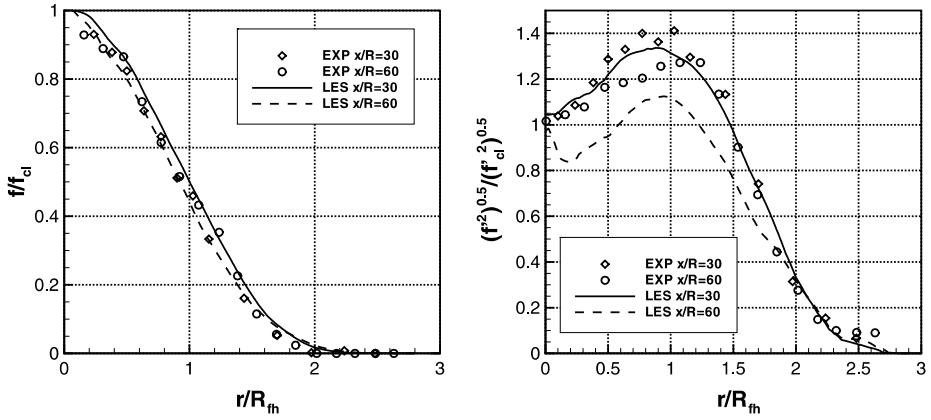

Fig. 5. Normalized radial profiles for a turbulent non-reacting C_3H_8, jet at different axial locations, left: mean mixture fraction f/f_{cl}, right: mixture fraction fluctuations.

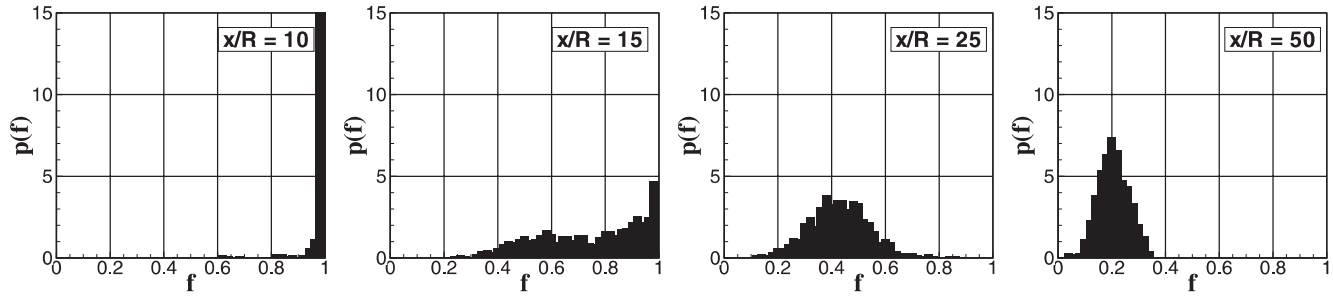

Fig. 6. Probability density distributions of the mean mixture fraction at different locations along the centerline of a turbulent non-reacting C_3H_8 jet.

region are reflected by the boundary condition, when they interact with the outer boundaries. To prevent those non-physical numerical reflections from contaminating the solution process a high grid stretching is applied in these regions. Nevertheless, the ability of the LES method to correctly predict the fluctuation profile is evident.

Probability density distributions of the mixture fraction $p(f)$ along the centerline are calculated for 800 time samples of the instantaneous flow field. The distributions in Fig. 6 satisfy

$$\int_0^1 p(f)\mathrm{d}f = 1. \tag{14}$$

Slightly upstream of the end of the laminar core at $x/R = 10$ the distribution consists mainly of one single peak at $f = 1$. At $x/R = 15$ the transition region starts. The distribution is widely spread and far from Gaussian. Further downstream the distribution shows the expected Gaussian profile, which is slowly shifted to lower values of f since the propane concentration decreases. The PDF shows the implemented LES to yield a highly accurate analysis of the mixing process.

5. Film cooling configuration

The size of the domain of integration of the JICF simulation is shown in Fig. 7. The dashed lines mark the outer boundaries of the computational domain. The cooling fluid is driven by a pressure gradient from a plenum into the boundary layer flow through a 30° streamwise inclined pipe. The origin of the frame of reference is located at the jet hole center. The coordinates X, Y, Z represent the streamwise, normal, and spanwise direction.

To mimic the flow parameters in a gas turbine a cooling fluid is injected from a complete row of jets into a turbulent flat plate boundary layer at a Mach number $Ma = 0.2$ and a local Reynolds number of $Re_\infty = 400{,}000$ based on the distance from the leading edge of the flat plate to the hole. This Reynolds number is kept constant for all film cooling simulations. The ratio of the local boundary layer thickness to the hole diameter is $\delta_0/D = 2$. The relevant flow parameters and the geometrical parameters are summarized in Table 2. The velocity, density, and mass flux ratio are defined as

$$\mathrm{VR} = \frac{u_j}{u_\infty}, \quad \mathrm{DR} = \frac{\varrho_j}{\varrho_\infty}, \quad \text{and} \quad \mathrm{MR} = \frac{\varrho_j u_j}{\varrho_\infty u_\infty}, \tag{15}$$

where the subscripts j and ∞ denote the jet and the cross-flow fluid. The mass flux is varied as three different velocity ratios are investigated VR = 0.1, 0.28 and 0.48. Two different values of the density ratio DR, an air-to-air injection

Table 2
Blowing ratios for the film cooling simulations

Case	VR	DR	MR
1	0.1	1	0.1
2	0.28	1	0.28
3	0.48	1	0.48
4	0.1	1.53	0.153
5	0.28	1.53	0.43

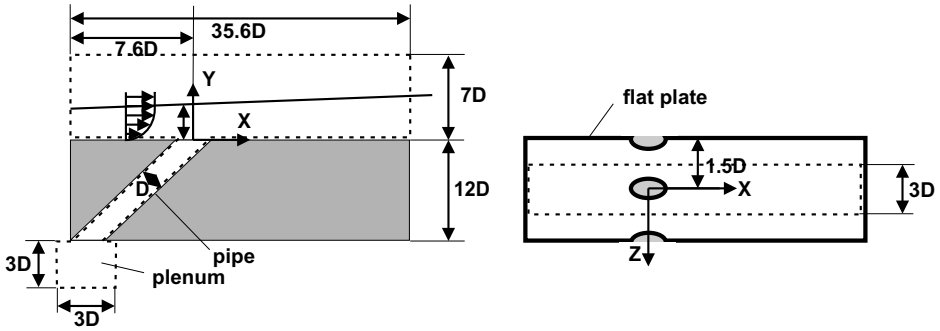

Fig. 7. Extension of the computational domain and flow configuration in the X–Y-plane (left) and the X–Z-plane (right).

with DR = 1 and a CO_2-to-air injection with DR = 1.53, are considered. All cases are listed in Table 2.

6. Boundary conditions

In large-eddy simulations of spatially developing boundary layers the treatment of the inflow boundary of the computational domain is one of the most intricate problems. In general and in particular in the JICF problem, the flow depends highly on the solution prescribed at the inlet.

The most physical approach to meet this challenge is to start to compute the flow right at the leading edge where the boundary layer emanates. However, the computational costs would be too extensive for the present problem. Tyagi and Acharya (2003) prescribed a turbulent profile and superimposed random fluctuations. On the one hand, this approach is based on minimum effort, on the other hand, it generates a slightly discontinuous solution, e.g., of the wall shear stress. Random perturbations are likely to be laminarized downstream. The flow can develop its own downstream turbulence independent of the random forcing, if the inflow boundary is located far upstream from the interaction region.

To avoid this problem an independent spatially developing boundary layer simulation is performed in the present work. Based on a slicing technique, the inflow distribution is prescribed using the velocity profile possessing the boundary layer parameters necessary at the inflow boundary of the jet-in-a-crossflow problem. The boundary conditions of the JICF simulation are sketched in Fig. 8.

The auxiliary flat plate flow simulation generates its own turbulent inflow data using the compressible rescaling method proposed by El-Askary et al. (2003, 2002). The rescaling method is a means of approximating the properties at the inlet via a similarity approach applied to the downstream solution. A detailed validation of this inflow generation method and its application to the JICF problem is given by Guo et al. (2006).

A sketch of the whole computational domain, which consists of the auxiliary domain, the JICF domain, a plenum, and a pipe, from which the cooling jet is injected into the crossflow, is shown in Fig. 8. In the spanwise direction full periodic boundary conditions are applied. Thus, an infinite row of staggered holes at a distance of $S = 3D$ between the centerlines is simulated. At the inlet of the plenum area the stagnation pressure is prescribed. The cooling fluid is driven through the pipe by the pressure difference between crossflow and plenum. The stagnation pressure is controlled by the calculation of the mass flux through the pipe to enforce a correct mass flux ratio. At the outer circumferential surface of the plenum the mass flux is assumed to vanish asymptotically.

The outflow boundary conditions are based on the conservation equations written in characteristic variables. To damp numerical reflections at the outflow boundaries sponge zones are introduced into the computational domain, as indicated in Fig. 8. In these regions source terms are superimposed on the right-hand side of the governing equations to drive the instantaneous solution of Q to a desired target solution Q_t, e.g., the logarithmic boundary layer profile. For further details see (Guo et al., 2006). The source terms are formulated as

$$S = \sigma(Q(t,\vec{x}) - Q_t(\vec{x})), \tag{16}$$

where the parameter σ is a polynomial function of the distance to the outflow boundary and decreases from σ_{max} to 0 within the boundary layer.

On the wall the no-slip conditions are prescribed, the pressure gradient is assumed to be negligible, and adiabatic conditions are imposed.

7. Computational details

All simulations have been performed on a block-structured mesh shown in Fig. 9. The grid consists of 5.65 million cells distributed over 24 blocks. The computational domain is enlarged by three additional blocks to perform an independent boundary layer simulation, which provides via an additional large-eddy simulation accurate instantaneous inflow data for the LES of the JICF problem. The grid points are clustered near the walls of the flat plate and the pipe. The minimum wall-normal distance of the

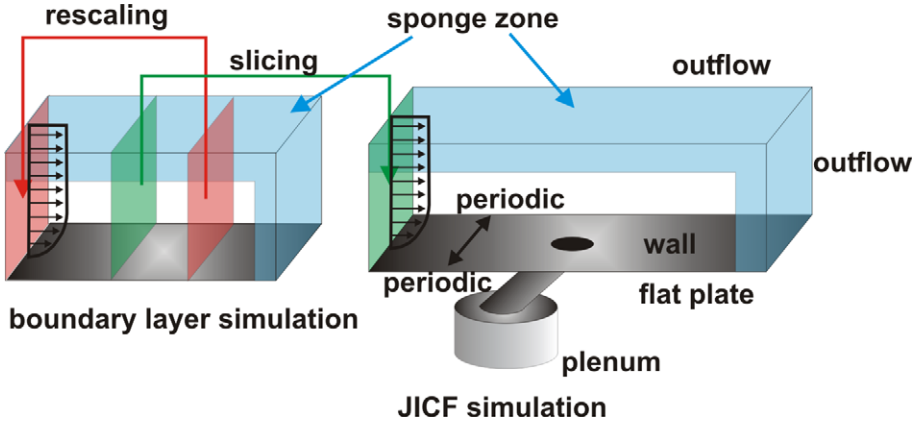

Fig. 8. Schematic of the computational domains and the boundary conditions of the JICF simulation.

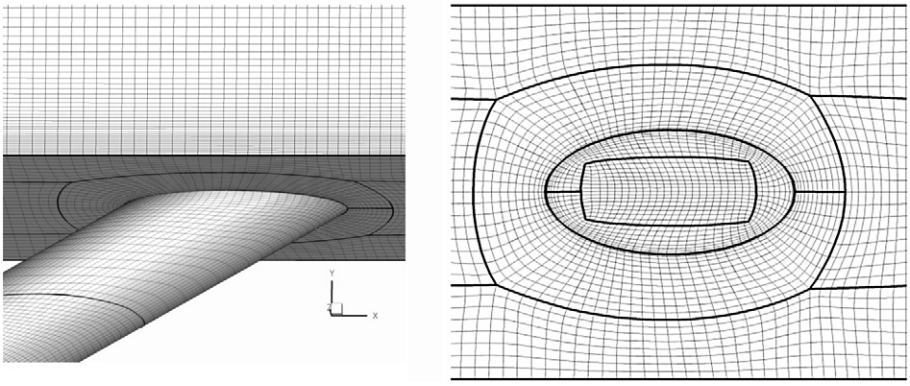

Fig. 9. Block-structured mesh used for the JICF simulation; left: 3d view of the pipe-plate junction; right: cross-section at $y/D = 0$; every second node is shown.

control volume on the flat plate has a dimension of $\Delta y = 0.004D$, which corresponds to $\Delta y^+_{\min} = 1.0$. In the area of high grid refinement near the jet hole edges the minimum streamwise and spanwise step sizes are $\Delta x^+_{\min} = 1.5$ and $\Delta z^+_{\min} = 1.5$. Grid stretching in the off wall region leads to $\Delta x^+ = 75$, $\Delta y^+ = 50$, and $\Delta z^+ = 12$.

The physical time step is $\Delta t = 0.02D/U_\infty$. To obtain the time-averaged statistics the flow field has been sampled over eight time periods. Here, one period is the time the crossflow fluid needs to pass over the length of the plate.

8. Results and discussion

The results are presented with the following structure. First, the mean flow field and the turbulent transport of the jet-crossflow interaction is discussed. Then, the impact of the velocity and the density ratio is analyzed. Next, the findings are compared with experimental data to show the quality of the computational method. Subsequently, the instantaneous mixing process is analyzed and the characteristic properties of the jet-crossflow interaction are explained. Finally, the cooling efficiency is studied by means of the mixture fraction distribution of the denser gas.

8.1. Mean flow field and turbulent transport

The flow field of the jet-crossflow interaction is discussed by the analysis of the time-averaged quantities of the mean velocity and the concentration field at a velocity ratio

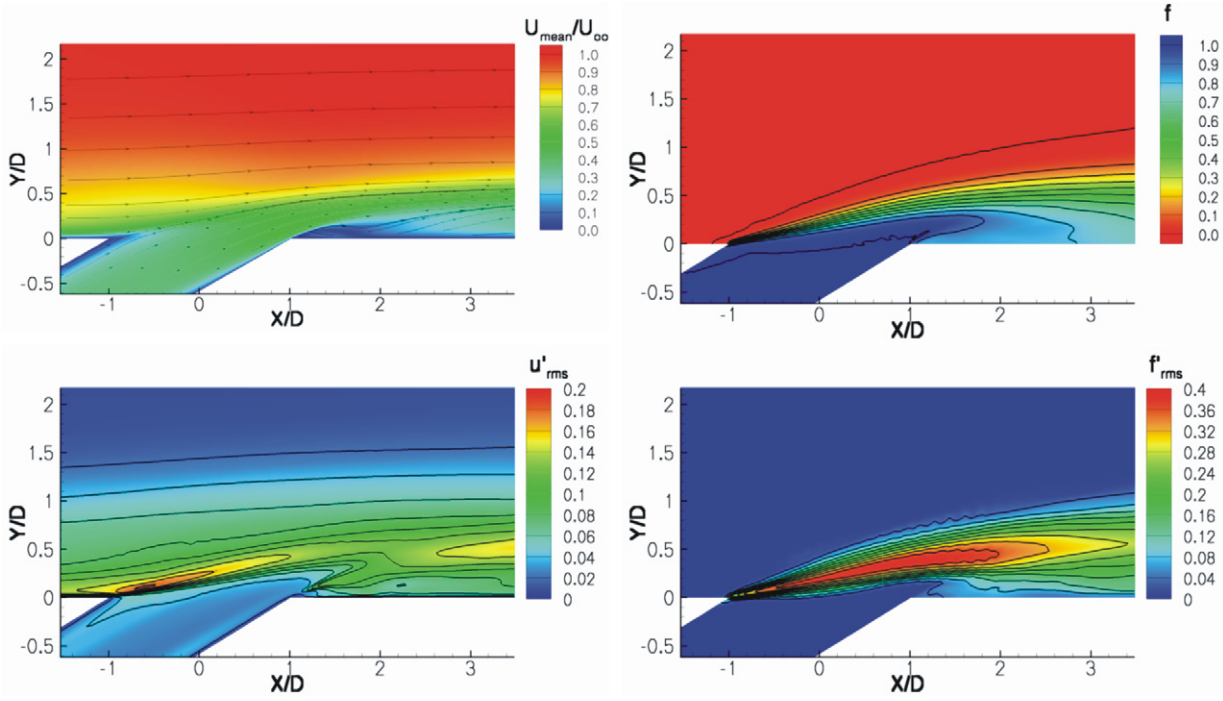

Fig. 10. Cross-section in the jet symmetry plane at VR = 0.28 and DR = 1.53, top left: mean velocity contours and streamlines, top right: contours of the mean mixture fraction f of the high density jet fluid, lower left: contours of the streamwise velocity fluctuation u'_{rms}, lower right: contours of the mixture fraction fluctuation f'_{rms}.

VR = 0.28 and a density ratio DR = 1.53, i.e., a CO_2 jet is injected into an air crossflow. In Fig. 10 the flow field in the vicinity of the jet hole is depicted in the symmetry plane at $Z/D = 0$. Streamlines and contours of the mean velocity $U_{mean}/U_\infty = \sqrt{u^2 + v^2 + w^2}/U_\infty$ characterize the resulting velocity field in Fig. 10 (top left). The jet is deflected by the crossflow at the leading edge of the jet exit. The maximum jet exit velocity is shifted to the trailing edge. The vertical velocity component causes a separation at the leeward side of the jet exit despite the low blowing ratio and strong inclination α. A distinct recirculation region can be identified, where the initial mixing between jet and crossflow takes place and the cooling efficiency is severely decreased.

The distribution of the mean mixture fraction f of the high density fluid (CO_2) is shown in Fig. 10 (top right). The separation of the jet downstream of the trailing edge is clearly visible by the shifting of the maximum of the cooling fluid concentration off the plate, such that low-density fluid is entrained between jet and surface. Further downstream, the jet-crossflow interaction leads to a growing dispersion of the cooling fluid.

The magnitude of the streamwise velocity fluctuation $u'_{rms} = (\overline{u'^2})^{1/2}/U_\infty$ in the jet symmetry plane is displayed in Fig. 10 (bottom left). The production of turbulence in the flow field characterizes the transport of momentum and thus, the dispersion of the cooling fluid. The first major zone of turbulence production is located at the jet leading edge. This is due to the large velocity gradient between the crossflow and the exiting jet. Note, the turbulence intensities increase due to the convergent character of the free shear flow. That is, the thickness of the free shear flow layer decreases downstream. High turbulence intensities also occur at the trailing edge between the jet and the separation zone as well as further downstream at $x/D = 3$ between the jet and the mainstream. All these areas mark zones of high shear in the mean flow field.

The dispersion of the cooling jet fluid is evidenced by the mixture fraction fluctuation $f'_{rms} = (\overline{f'^2})^{1/2}$ of the high density jet fluid in Fig. 10 (bottom right). The maximum fluctuation levels are limited by $f'_{rms} = 0.4$ and are located in the turbulent shear zone emanating from the leading edge of the jet hole. This area coincides with the region of the largest gradients in the mean mixture fraction scalar field.

Figs. 11 and 12 show the evolution of vortical structures and the mixing process due to the interaction of the turbulent boundary layer with the high density cooling jet-in the Y–Z-plane at various X/D locations. The streamwise vorticity magnitude Ω_x is juxtaposed with the distribution of the mixture fraction f at each cross-section. Vectors of the secondary velocity field are added to emphasize the location and extension of the vortical structures in the mean flow field. The locations of the cross sections at $X/D = -1, 0, 0.75, 1, 1.5$, and 2 are visualized in the upper subfigures of Fig. 11 and 12, respectively. The streamlines show the deflection of the crossflow by the jet and the swirling motion of the jet fluid being entrained by the crossflow.

At the windward edge of the jet exit, which coincides with the streamwise coordinate $X/D = -1$, the impact of the cooling jet injection on the turbulent boundary layer is still very weak. The magnitude of the averaged streamwise vorticity and the mixture fraction f is nearly zero. However, the velocity vectors show the beginning deflection of the crossflow.

At $X/D = 0$, i.e., at the intersection of the pipe centerline and the flat plate surface, the cooling fluid is diffused in the lateral and the wall-normal direction into the mainstream. The jet exit velocity is increased. The shear between the jet and the crossflow induces vorticity at the jet hole edges. The vortex pair that possesses a counter-rotating orientation governs the flow field downstream of the jet exit. The boundary layer fluid starts to roll-up at the lateral edges of the hole with an orientation that is opposite to that of a standard horseshoe vortex. This mechanism is discussed at length in Section 8.4 *Characteristics of the jet-crossflow interaction*. The mismatch in vertical momentum between the jet and the crossflow results in vorticity of opposite orientation at both edges (Peterson and Plesniak, 2004). The deflected boundary layer entrains cooling fluid in a swirling motion.

At $X/D = 0.75$ the streamwise vorticity generated at the jet hole edges is more pronounced and the counter-rotating vortex pair (CVP) starts to develop above the plate. The mutual deflection of jet and crossflow adds a lateral component to the jet velocity such that the cooling fluid penetrates deeper into the mainstream in the lateral and wall-normal direction. However, the strong vortical structures cause low-density mainstream fluid to get mixed beneath the jet and the plate yielding a reduced cooling efficiency.

In Fig. 12 the flow field downstream of the jet exit is emphasized by another three cross-sections. At $x/D = 1.0$ the CVP is already fully developed and is slightly lifted off the plate. Note, the mixture fraction f directly at the wall is already severely reduced by the entrainment of mainstream fluid. The mixing between both fluids follows the development of the vortex pair. The cross-sections at $x/D = 1.5$ and $x/D = 2.0$ show the continuing dispersion of the jet fluid. The diameters of the CVP grow while the vorticity magnitude decreases. The maximum values of the mixture fraction f mark the center of the cooling jet. This center is lifted off the wall as low-density fluid from the mainstream is entrained between the wall and the jet by the CVP. In the downstream direction the mutual induction reduces the distance between the CVP centers and increases the distance to the wall.

8.2. Impact of the density and the velocity ratio

To figure out the impact of the velocity ratio and the density ratio on the cooling efficiency, the parameters VR and DR are varied in the large-eddy simulations. In Figs. 13a–c Mach number contours and streamlines are shown in the JICF symmetry plane for three different cases. The illustrations in (a) and (b) evidence that a variation of the

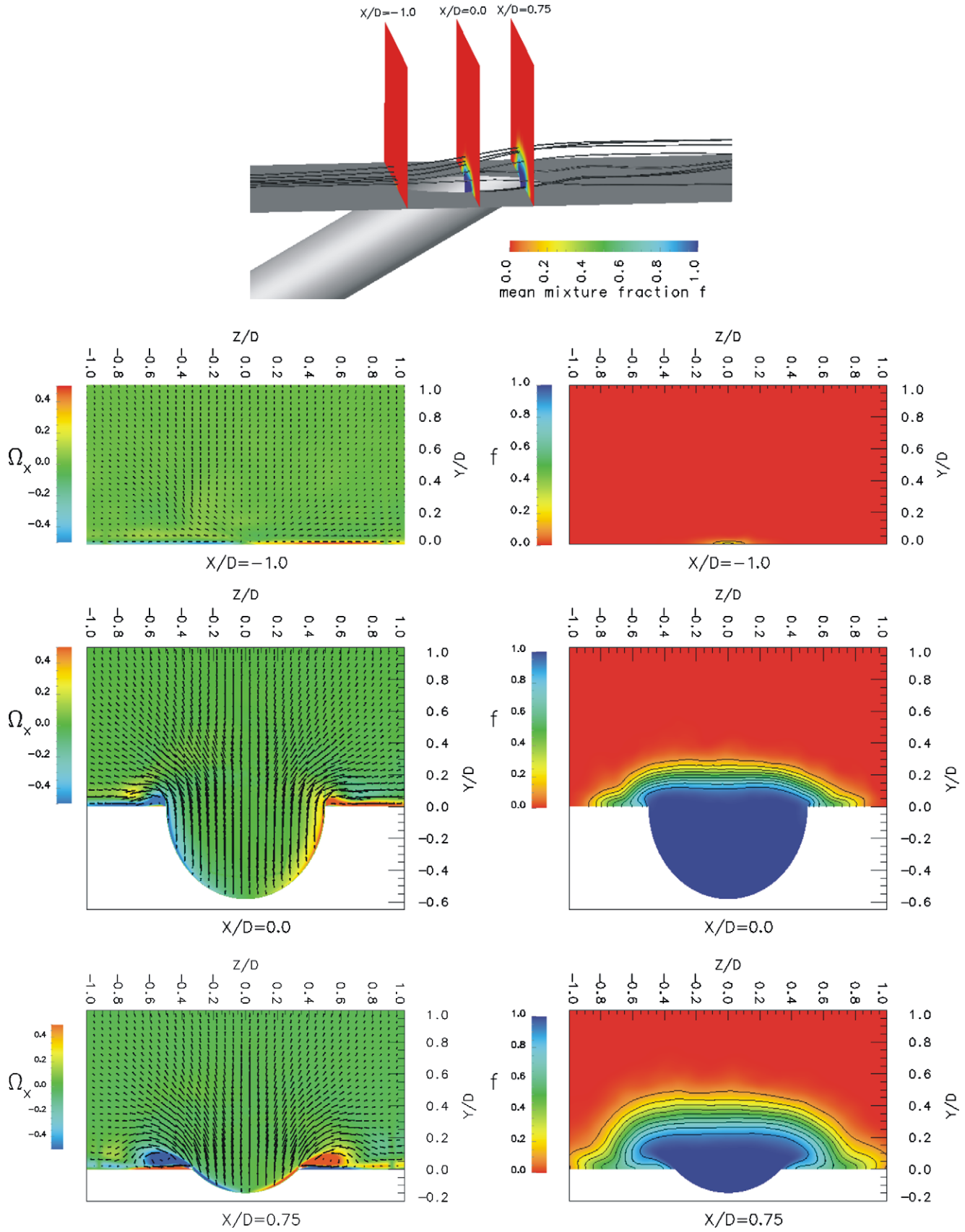

Fig. 11. VR = 0.28 and DR = 1.53, cross-sections at $X/D = -1$, 0, 0.75, top: 3d view and streamlines, left: streamwise vorticity Ω_x and vectors of the secondary velocity field, right: contours of the mean mixture fraction f.

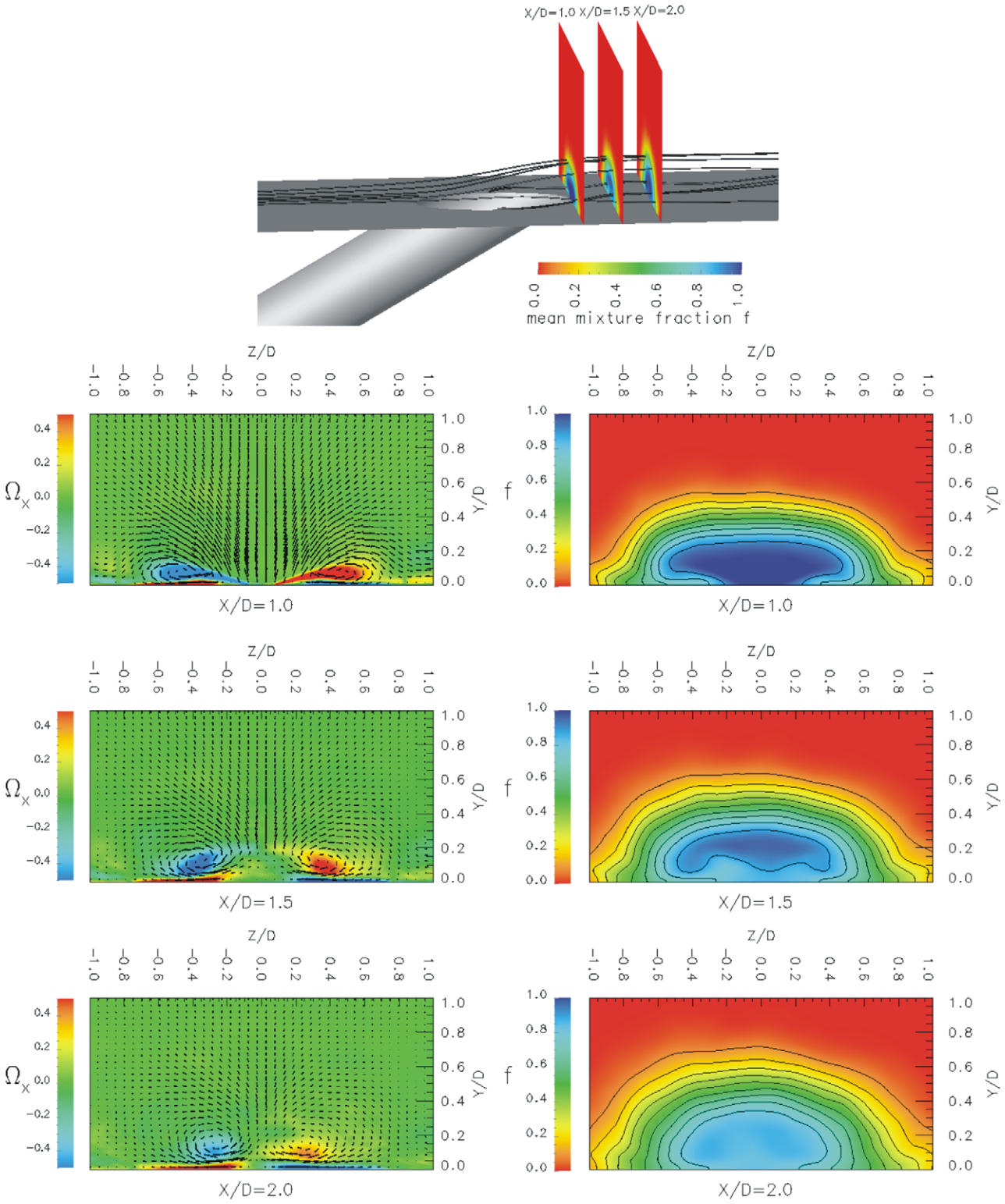

Fig. 12. VR = 0.28 and DR = 1.53, cross-sections at $X/D = 1,1.5,2$, top: 3d view and streamlines, left: streamwise vorticity Ω_x and vectors of the secondary velocity field, right: contours of the mean mixture fraction f.

velocity ratio has a large impact on the separation and reattachment behavior as well as the strength of the penetration into the crossflow.

On the other hand, a variation of the density ratio at a constant velocity ratio, which is shown in Figs. 13a and c, has only a minor effect on the dynamics of the flow field in the vicinity of the jet hole. The size of the recirculation region, the wall-normal velocity gradients, and the penetration depth possess only small differences if the velocity ratio is kept constant. However, the lateral spreading of the jet

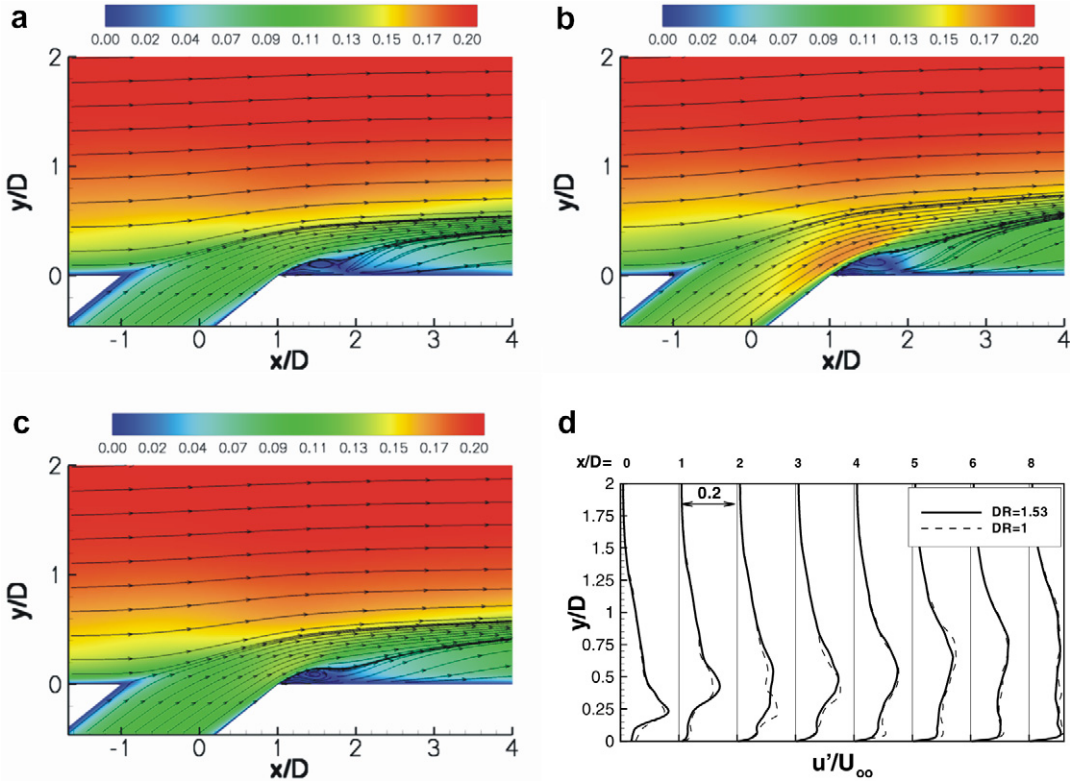

Fig. 13. Mach number contours in the JICF symmetry plane and streamlines (a) at VR = 0.28 and DR = 1, (b) at VR = 0.48 and DR = 1, (c) at VR = 0.28 and DR = 1.53, (d) profiles of the streamwise velocity fluctuation u'_{rms} for DR = 1 and DR = 1.53 at different X/D locations.

fluid is slightly increased at a higher jet density. This result agrees with the conclusion reported in Pietrzyk et al. (1990).

The same behavior is observed when turbulence intensities are considered. Profiles of the streamwise velocity fluctuation u'_{rms} at different X/D locations are shown in Fig. 13(d) at VR = 0.28 and two density ratios DR = 1 and DR = 1.53. The wall-normal distribution and the peak levels almost match at both density ratios. This is to be expected as the velocity gradients in the mean flow field are almost identical.

8.3. Comparison of numerical and experimental results

Particle-image velocimetry (PIV) measurements of jets in a crossflow have been conducted by Jessen et al. (in press). The flow parameters of the experimental investigations match exactly those of the present numerical simulations.

In Fig. 14 profiles of the streamwise velocity are shown for two density ratios (DR = 1, DR = 1.53) and two velocity ratios VR = 0.1 and VR = 0.28. The profiles are illustrated in the spanwise symmetry plane ($Z/D = 0$) at different streamwise locations ($X/D = -1$, 0, 1, 1.5, and 2). The location $X/D = -1$ corresponds to the upstream edge of the jet hole, where the lifting effect of the jet on the boundary layer is still very small and the velocity profile is close to the fully developed turbulent profile of a flat plate at the corresponding Reynolds number. At $X/D = 0$ and $X/D = 1$ the boundary layer is lifted and the jet penetrates into the crossflow. In the case of the higher velocity ratio the negative streamwise velocity near the wall at $X/D = 1.5$ emphasizes the separation region. The jet is already reattached at $X/D = 2$. In all four cases the predicted flow field is in excellent agreement with the PIV measurements. Small deviations only occur near the jet hole edges and close to the wall below $Y/D = 0.1$, where the PIV measurements are affected by laser light reflections. The velocity field in the vicinity of the jet injection is very similar for both density ratios.

The average of the wall-normal velocity component near the jet hole exit is shown in Fig. 15. At different X-axis locations profiles of the wall-normal velocity component are shown for the high density ratio case at VR = 0.1 and VR = 0.28. At $X/D = -1$ the averaged wall-normal velocities are caused by the growth of the boundary layer. In the jet hole center at $X/D = 0$ the lifting movement of the jet increases the wall-normal velocity. The maximum values occur near $X/D = 1$, where the vector of the jet velocity is almost parallel to the inclination angle. Although the wall-normal component is about one order of magnitude smaller than the streamwise component, the numerical findings match the measurements very well except in the immediate vicinity of the wall, where the measurements are strongly affected by reflections.

To visualize the instantaneous flow patterns contours of the streamwise velocity and normalized velocity vectors are shown in Fig. 16 in the jet symmetry plane. A direct comparison of the measured (left) and computed (right) flow

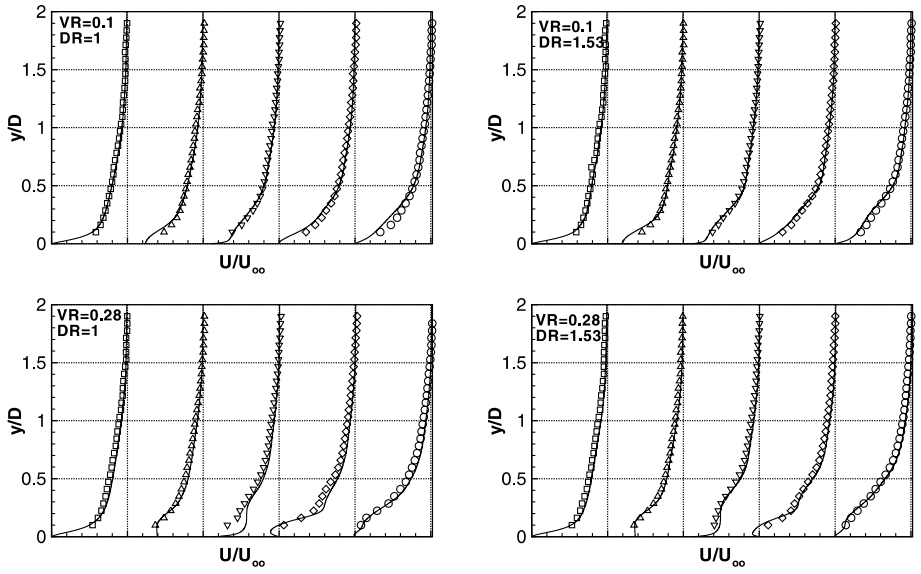

Fig. 14. Profiles of streamwise velocity in the symmetry plane at different streamwise locations, top left: VR = 0.1, DR = 1, bottom left: VR = 0.28, DR = 1, top right: VR = 0.1, DR = 1.53, bottom right: VR = 0.28,DR = 1.53, experimental data (□) $x/D = -1$, (△) $x/D = 0$, (▽) $x/D = 1$, (◇) $x/D = 1.5$, (○) $x/D = 2$, and solid lines: LES data.

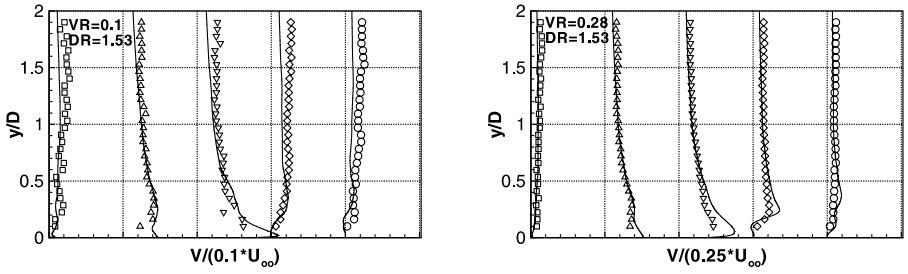

Fig. 15. Profiles of the wall-normal velocity component in the symmetry plane at different streamwise locations, left: VR = 0.1, DR = 1.53, right: VR = 0.28, DR = 1.53, experimental data (□) $x/D = -1$, (△) $x/D = 0$, (▽) $x/D = 1$, (◇) $x/D = 1.5$, (○) $x/D = 2$, and solid lines: LES data.

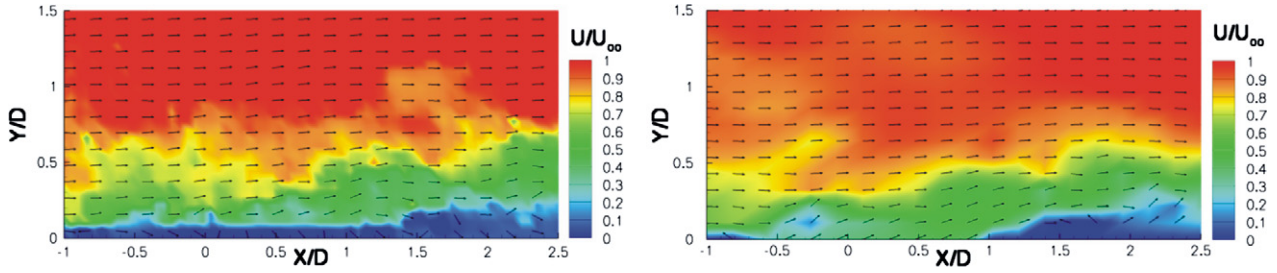

Fig. 16. Instantaneous flow field in the spanwise symmetry plane at VR = 0.28, DR = 1.53, contours of streamwise velocity and normalized velocity vectors, left: PIV, and right: LES; note, strong reflections prevent the viscous sub-layer to be resolved in the PIV measurements.

field at VR = 0.28 and DR = 0.28 demonstrates the high quality of the data. It is evident that the turbulent structures in the boundary layer, the velocity field of the penetrating jet fluid above the hole, and the location as well as the height of the recirculation region agree very well. Note, the PIV measurements in the region $Y/D < 0.1$ suffer from strong reflections from the wall surface.

The mixing diffusion of the cooling fluid is significantly influenced by the turbulence. Therefore, to correctly simulate the mixing process in the near field and downstream of the jet hole, the turbulence intensity has to be accurately predicted. In Fig. 17 contours of the root mean square (rms) of the streamwise velocity fluctuation $u'_{\mathrm{rms}} = (u'^2)^{\frac{1}{2}}/U_\infty$ are displayed at $Z/D = 0$ for the high density case and VR = 0.28. At this low blowing ratio there are two major zones of turbulence production. The first domain is located inside the shear layer between the jet and the crossflow due to the mismatch of streamwise momentum (Walters and Leylek, 2000). The second zone of high turbulence is located above the wake of the jet hole and marks the initial mixing

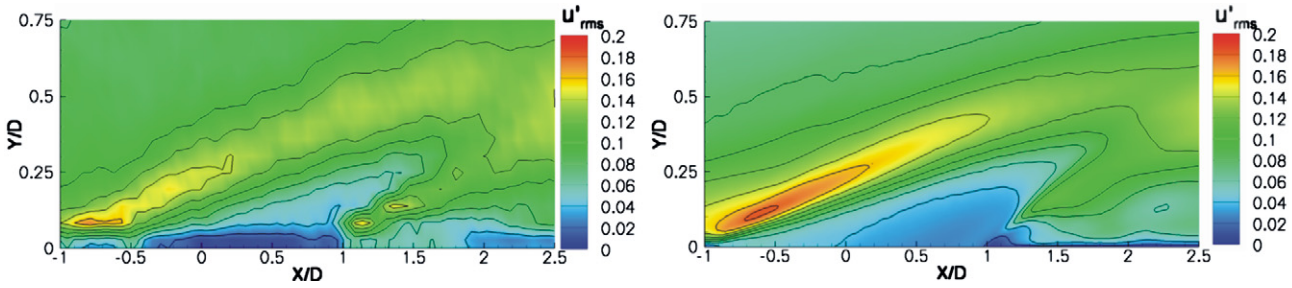

Fig. 17. Contours of the streamwise velocity fluctuation u'_{rms} at VR = 0.28, DR = 1.53, left: PIV, and right: LES.

of the jet fluid and the boundary layer flow. In Fig. 17 u'_{rms} PIV and LES data are juxtaposed. It is obvious that the aforementioned turbulence production zones are correctly predicted by the numerical simulation. The distribution and the overall strength of the turbulence intensity matches the experimental findings very well.

A quantitative comparison of the turbulence level in the PIV and LES findings is given in Fig. 18. At several X-axis locations profiles of the u'_{rms} value are illustrated. The numerical data (solid lines) are in convincing agreement with the measured results (symbols) in the lower part of the boundary layer. In the upper part of the boundary layer stronger deviations occur. It is conjectured that this discrepancy is caused by two reasons. First, the freestream turbulence in the measurements is higher than in the numerical simulation. Second, the PIV measurement system was calibrated to measure the higher turbulence right in the vicinity of the wall surface (Jessen et al., in press). Since the turbulence level right adjacent to the surface is completely different from that in the outer region, the accuracy of the data measured by the experimental setup is reduced in the outer region. In other words, it is assumed that the mismatch in the outer zone is due to poor measurement data and not caused by the LES solution. At $X/D = 0$ in the jet hole center the shear zone between jet and crossflow is clearly visible. Further downstream at $X/D = 1$ this zone is lifted as the jet penetrates into the boundary layer. At $X/D = 1.14$ the shear zone between wake and jet is clearly resolved by the LES and PIV approaches. Finally, at $X/D = 2$ both initial shear zones are diffused and the turbulence intensities form a bulkier profile that marks the highly unsteady mixing in the CVP region, which can be considered fully developed in the streamwise direction.

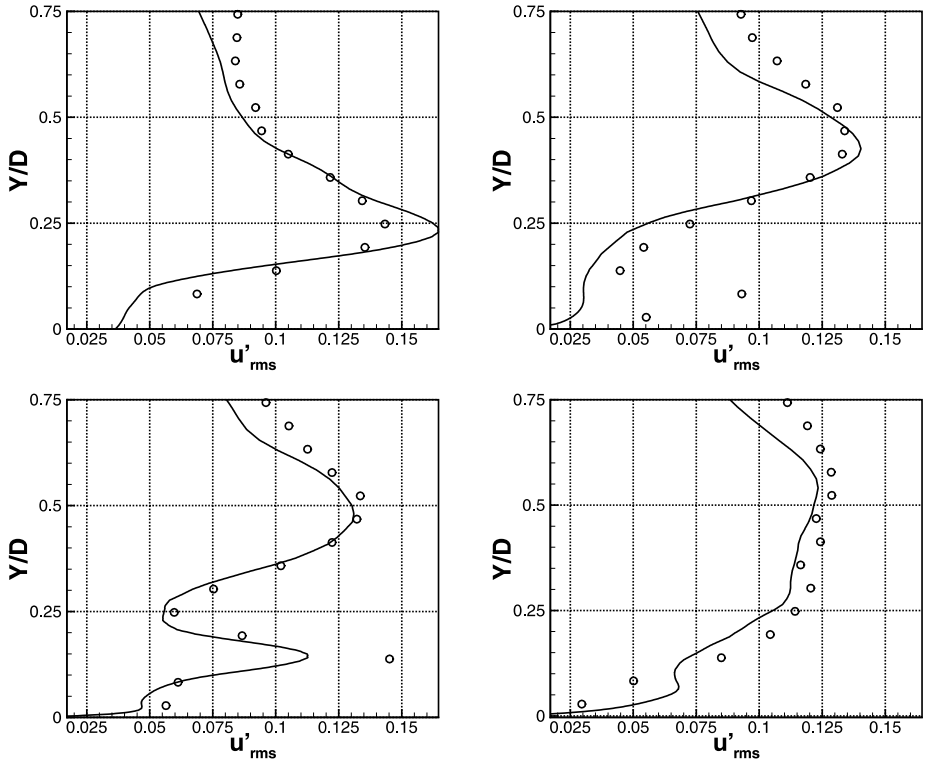

Fig. 18. Profiles of streamwise velocity fluctuations u'_{rms} at VR = 0.28, DR = 1.53, top left: $X/D = 0$, top right: $X/D = 1$, bottom left: $X/D = 1.14$, bottom right: $X/D = 2$, experimental data: (○), and LES data: solid line.

8.4. Characteristics of the jet-crossflow interaction

The turbulent mixing process of the different species is dominated by the formation of the counter-rotating vortex pair (CVP) downstream of the jet hole. There are different explanations for the generation of the CVP, e.g., those from Kelso et al. (1996) or Morton and Ibbetson (1995). The present study is closely related to the hypothesis discussed in detail by Peterson and Plesniak (2004). They state the reason for the initial formation of the CVP to be the shearing of the boundary layer fluid by the jet.

Due to the high resolution as well as the time accuracy of the present numerical scheme and the possibility to track the passive mixture fraction scalar, a detailed analysis of the formation of the CVP and the initial mixing process can be performed. In Fig. 19 the contours of the mixture fraction f and the vectors of the secondary velocity field at the same instantaneous time level are shown in two cross-sections at $X/D = 1$, i.e., directly at the trailing edge of the hole, and further downstream at $X/D = 1.5$. The velocity ratio is VR = 0.28 and the density ratio is DR = 1.53.

It goes without saying that there is already vorticity in the boundary layer. This vorticity distribution is definitely altered when the boundary layer flow encounters a sharp edge. This is the case at the film cooling hole. Even when there is no jet, i.e., the hole can be considered some kind of cavity, additional vortices are generated near the wall. Without any jet flow this additional vorticity is similar to that of a horseshoe vortex, which is generated when the boundary layer flow encounters a solid obstacle. That is, these edge-driven vortices would have the same orientation as a horseshoe vortex. When the jet is injected with a positive wall-normal momentum even more vorticity is added to the boundary layer flow. At a sufficiently high momentum the rotation of the vortices is determined by the jet speed, i.e, the counter-rotating vortices rotate in the opposite direction compared with a horseshoe vortex. The location of the counter-rotating vortex pair, i.e., primarily its position normal to the surface and its strength, depends on the momentum ratio of the jet and the outer flow. In brief, compared to an unperturbed boundary layer flow the vorticity in a jet-in-a-crossflow problem is increased by the discontinuities due to the edges of the hole and the momentum ratio.

Fig. 19 evidences that the eddies generated by the jet-crossflow interaction are already lifted off the plate at $X/D = 1$. The mixture fraction f on the plate wall is reduced as crossflow fluid is entrained under the jet by the large-scale vortices. Further downstream, in the zone being governed by oscillating separation and reattachment, the vortical structures possess a smaller scale. They are more intense and more intricate and as such the mixing process is accelerated.

The separation-reattachment zone can be identified in Fig. 20. The mixture fraction f is shown at an instantaneous time level in the streamwise symmetry plane. On the right, coherent structures indicated by the λ_2 criterion (Jeong and Hussain, 1995) with mapped-on mixture fraction distribu-

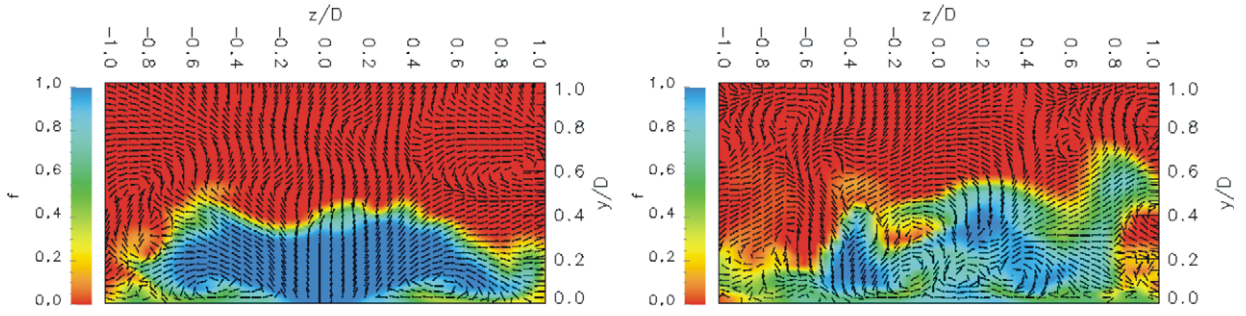

Fig. 19. Instantaneous mixture fraction contours and velocity vectors at $X/D = 1$ (left) and $X/D = 1.5$ (right), VR = 0.28, and DR = 1.53.

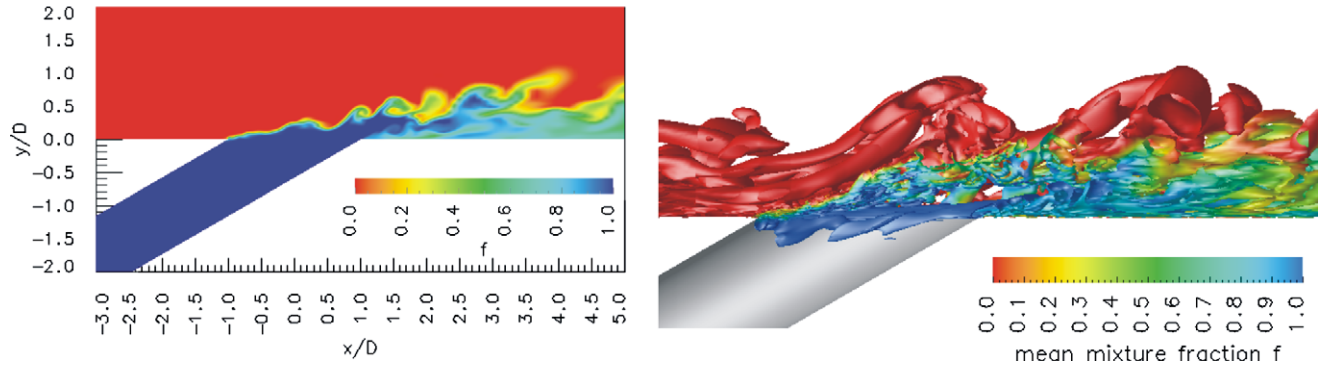

Fig. 20. Left: Instantaneous contours of the mixture fraction f in the symmetry plane at a velocity ratio of VR = 0.28 and DR = 1.53, right: coherent structures indicated by the λ_2 criterion with mapped on mixture fraction f.

tion f are depicted. The illustrations in Fig. 20 visualize the interaction of the inherent hairpin vortices of the turbulent boundary layer with the effusing jet fluid. The hairpin-like structures in the upper part of the boundary layer are lifted and entrain jet flow fluid only after they have passed the trailing edge. The lower part of the boundary layer is deflected by the blockage effect of the jet. The small scale structures lead to the initial mixing in the shear zones. Further downstream, the mixing process is significantly accelerated in the separation region.

8.5. Cooling efficiency

Following the heat-mass transfer analogy the penetration of the CO_2 jet into an air crossflow mimics the density ratio between the cooling fluid and the hot boundary layer flow in a gas turbine. Hence, the distribution of the mean mixture fraction f along the flat plate downstream of the jet hole resembles the film-cooling efficiency. The contours of the mixture fraction f along the plate at two different velocity ratios VR = 0.1 and VR = 0.28, respectively, and a density ratio of DR = 1.53 yielding the mean flux ratios MR = 0.153 and MR = 0.43 are shown in Fig. 21. The coverage of the plate is significantly improved at a higher mass flux ratio. The lower figure on the left shows a stronger lateral spreading of the dense fluid and higher peak values that exist further downstream.

Furthermore, the mean mixture fraction f along the plate centerline as a function of the streamwise coordinate is shown in Fig. 21 for the mass flux ration MR = 0.43. The data is compared with the experimental findings of Sinha et al. (1991). The symbols represent the measured film cooling efficiency η, which is a temperature based variable. The mass fraction of the dense gas is related to the cooling efficiency for the analogous heat transfer situation, i.e., $\eta = f$ as stated in Pedersen et al. (1977). In the experiments the density ratio is DR = 2 and VR = 0.25, which leads to a slightly higher mass flux ratio of MR = 0.5. Nevertheless, from the juxtaposition in Fig. 21 it can be concluded that the good agreement between both curves shows the mixture fraction distribution along the plate to correctly predict the film cooling efficiency of such flow configurations.

9. Conclusion

A method is presented to perform large-eddy simulations of the mixing between non-reacting gas species. The method is validated by predicting the turbulent mixing of a propane jet-in coflowing air. The LES method is used to investigate in detail the impact of the velocity ratio and the density ratio of the coolant and the outer fluid on the physics of film cooling flows. The numerical results are compared with experimental findings which are based on exactly the same flow parameters as were used in the computational analysis. The LES predictions for the velocity distributions are in excellent agreement with the available experimental data.

The high resolution of the computational domain, the time accuracy, and the possibility to track the passive mixture fraction scalar f of the cooling fluid allows a detailed analysis of the mean and the instantaneous flow field. Variations of the velocity ratio parameter significantly impact the flow field with respect to the dynamic separation and reattachment process, the turbulence statistics, and the cooling efficiency, whereas a variation of the density ratio has only a minor influence, if the velocity ratio is kept constant.

The flow physics is discussed by identifying the dominant vortical structures. The cooling efficiency along the flat plate is identified by the mean mixture fraction distribution. Comparisons with findings from the literature convincingly show the validity of the heat-mass transfer analogy to investigate such flows. The evaluation of the cooling efficiency is dominated by density effects. Thus,

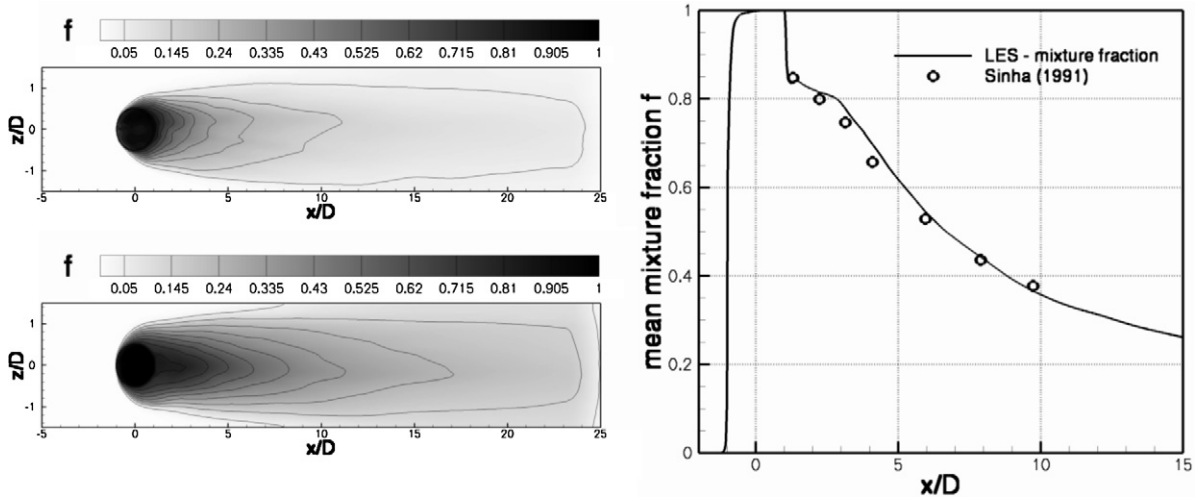

Fig. 21. Left: contours of the mean mixture fraction f along the flat plate at MR = 0.153 (top) and at MR = 0.43 (bottom); right: mean mixture fraction along the centerline at MR = 0.43 compared with the film cooling efficiency η measured at MR = 0.5 by Sinha et al. (1991).

the prediction of the cooling efficiency cannot be based on just considering the velocity ratio. The density ratio has to be taken into account to gain reliable results, i.e., the mass flux ratio is the parameter which determines the cooling efficiency.

Acknowledgements

The support of this research by the Deutsche Forschungsgemeinschaft (DFG) in the framework of the Collaborative Research Center 561 and the High Performance Computing Center Stuttgart (HLRS) is gratefully acknowledged.

References

Alkishriwi, N., Meinke, M., Schröder, W., 2006. A large-eddy simulation method for low Mach number flows using preconditioning and multigrid. Comput. Fluids 35 (10), 1126–1136.

Andreopoulus, J., Rodi, W., 1984. Experimental investigation of jets in a crossflow. J. Fluid Mech. 138, 93–127.

Barlow, R.S., 1998. In: Proccedings of the third international workshop on measurements and computation of turbulent nonpremixed flames. Tech. Rep. URL: <http://www.ca.sandia.gov/tnf/>.

Bernsdorf, S., Rose, M., Abhari, R., 2006. Modeling of film cooling. Part I. Experimental study of flow structure. ASME J. Turbomach. 128, 141–149.

Bird, R.B., Stewart, W.E., Lightfoot, E.N., 1960. Transport Phenomena. John Wiley and Sons Inc..

Bogey, C., Bailly, C., 2003. Les of high reynolds, high supersonic jet: effects of the inflow conditions on flow and noise. AIAA Paper. pp. 2003–3170.

Bogey, C., Bailly, C., Juve, D., 2002. Noise investigation of a high subsonic moderate reynolds number jet using a compressible large eddy simulation. Theor. Comput. Fluid Dyn. 16, 273–297.

Burdet, A., Abhari, R., Rose, M., 2005. Modeling of film cooling. Part II. Model for use in 3d CFD. ASME Paper. pp. GT2005-68780.

Dibble, R.W., Harmann, V., Schefer, R.W., Kollmann, W., 1987. Conditional sampling of velocity and scalars in turbulent flames using simultaneous LDV-Raman scattering. Exp. Fluids 5 (2), 103–113.

El-Askary, W., Schröder, W., Meinke, M., 2003. LES of compressible wall-bounded flows. AIAA Paper. pp. 2003–3554.

Ewert, R., Schröder,W., Meinke, M., El-Askary, W., 2002. LES as a basis to determine sound emission. AIAA Paper. pp. 2002–0568.

Fureby, C., Grinstein, F.F., 1999. Monotonically integrated large eddy simulation of free shear flows. AIAA J 37, 544–556.

Goldstein, R.J., Eckert, E.R.G., Burggraf, F., 1974. Effects of hole geometry and density on three-dimensional film cooling. Int. J. Heat Mass Transfer 17 (5), 595–607.

Grinstein, F.F., Fureby, C., 2002. Recent progress on MILES for high Reynolds number flows. J. Fluids Eng. 124, 848–861.

Guo, X., Schröder, W., Meinke, M., 2003a.LES of film cooling. In: Proceedings of the International Gas Turbine Congress, Tokyo, 2003a. Paper IGTC 2003 TS-06.

Guo, X., Meinke, M., Schröder, W., 2003b. Large-eddy simulation of a jet in a crossflow. In: Geurts, B., Friedrich, R., Metais, O. (Eds.), Direct and Large-Eddy Simulation V. Kluwer, pp. 603–610.

Guo, X., Meinke, M., Schröder, W., 2004. Flow prediction for film cooling by large-eddy simulation. In: Proceedings of the10th of International Symposium on Transport Phenomena and Dynamics of Rotating Machinery, Honolulu. Paper 157.

Guo, X., Meinke, M., Schröder, W., 2006. Large-eddy simulation of film cooling flows. Comput Fluids 35, 587–606.

Gustafsson, K.M.B., Johansson, T.G., 2006. Numerical simulation of effusion cooling with comparisons to experimental data, progress in computational fluid dynamics. Inter. J. 6 (1–3), 101–109.

Hoda, A., Acharya, S., 2000. Predictions of a film coolant jet in crossflow with different turbulence models. ASME J. Turbomach. 122, 558–569.

Iourokina, I., Lele, S.K., 2006. Large eddy simulation of film-cooling above the flat surface with a large plenum and short exit holes. AIAA Paper. pp. 2006-1102.

Jeong, J., Hussain, F., 1995. On the identification of a vortex. J. Fluid Mech. 285, 69–94.

Jessen, W., Schröder, W., Klaas, M., in press. Evolution of jets effusing from inclined holes into crossflow. Int. J. Heat Fluid Flow, doi:10.1016/j.ijheatfluidflow.2007.06.010.

Kelso, R.M., Lim, T.T., Perry, A.E., 1996. An experimental study of round jets in crossflow. J. Fluid Mech. 306, 111–144.

Mathur, S., Tondon, P.K., Saxena, S.C., 1967. Thermal conductivity of binary, ternary and quarternary mixtures of rare gases. Mol. Phys. 12, 569.

Meinke, M., Schröder, W., Krause, E., Rister, T., 2002. A comparison of second- and sixth-order methods for large-eddy simulations. Comput. Fluids 31, 695–718.

Morton, B.R., Ibbetson, A., 1995. Jets deflected in a crossflow. Exp. Therm. Fluid Sci. 12, 112–133.

Muldoon, F., Acharya, S., 2006. Analysis of $k-\epsilon$ Budgets for Film Cooling Using Direct Numerical Simulation. AIAA J 44 (12), 3010–3021.

Pedersen, D.R., Eckert, E.R.G., Goldstein, R.J., 1977. Film cooling with large density differences between the mainstream and the secondary fluid measures by the heat-mass transfer analogy. ASME J. Turbomach. 99, 620–627.

Peterson, S.D., Plesniak, M.W., 2004. Evolution of jets emanating from short holes into crossflow. J. Fluid Mech. 503, 57–91.

Pietrzyk, J.R., Bogard, D.G., Crawford, M.E., 1990. Effects of density ratio on the hydrodynamics of film cooling. ASME J. Turbomach. 112, 437–443.

Plesniak, M., Cusano, D., 2005. Scalar mixing in a confined rectangular jet in a crossflow. J. Fluid Mech. 524, 1–45.

Renze, P., Meinke, M., Schröder, W., 2006. LES of turbulent mixing in film cooling flows. In: Proceedings of the Conference on Turbulence and Interactions. Porquerolles, France.

Renze, P., Schröder, W., Meinke, M., 2007. Hole shape comparison for film cooling flows using large-eddy simulations. AIAA Paper. pp. 2007–0927.

Rütten, X., Meinke, M., Schröder, W., 2005. Large-eddy simulation of low frequency oscillations of the Dean vortices in turbulent pipe bend flows. Phys. Fluids 17, 035107.

Schefer, R.W., Dibble, R.W., 2001. Mixture fraction field in a turbulent non-reacting propane jet. AIAA J. 39 (1), 64–72.

Shur, M.L., Spalart, P.R., Strelets, M.K., Travin, A., 2003. Towards the prediction of noise from jet engines. Int. J. Heat Fluid Flow 24, 551–561.

Sinha, A.K., Bogard, D.G., Crawford, M.E., 1991. Film-cooling effectiveness downstream of a single row of holes with variable density ratio. ASME J. Turbomach. 113, 442–449.

Tucker, P.G., 2004. Novel MILES computations for jet flows and noise. Int. J. Heat Fluid Flow 25 (4), 625–635.

Turkel, E., 1999. Preconditioning techniques in computational fluid dynamics. Annu. Rev. Fluid Mech. 31, 385–416.

Tyagi, M., Acharya, S., 2003. Large eddy simulation of film cooling flow from an inclined cylindrical jet. ASME J. Turbomach. 125, 734–742.

Walters, D.K., Leylek, J.H., 2000. A detailed analysis of film-cooling physics. Part I. streamwise injection with cylindrical holes. ASME J. Turbomach. 122, 102–112.

Wilke, C.R., 1950. A viscosity equation for gas mixtures. J. Chem. Phys. 18, 517.